J. Am. Chem. Soc. 1988, 110, 7610-7616

# Excited States of Titanium(2+): Sharp-Band and Broad-Band Near-Infrared Luminescence from $Ti^{2+}$ in $MgCl_2$ and $MgBr_2$

**Stuart M. Jacobsen,[†] Hans U. Güdel,*[,†] and Claude A. Daul[‡]**

*Contribution from the Institut für Anorganische Chemie der Universität Bern, Freiestrasse 3, CH-3000 Bern 9, Switzerland, and Institut de Chimie Inorganoique, Universitê de Fribourg, Pêrolles, CH-1700 Fribourg, Switzerland.* *Received March 24, 1988*

**Abstract:** Single-crystal luminescence and absorption spectra of $Ti^{2+}(3d^2)$ doped into the host lattices $MgCl_2$ and $MgBr_2$ are presented. In the chloride, sharp-band near-infrared (near-IR) emission is observed at low temperatures with a radiative decay time of 109 ms. This sharp emission leads to a very accurate determination of the energy splitting within the $^3T_{1g}$ ($O_h$) ground state of $Ti^{2+}$ in this crystal environment, which is the result of trigonal field and spin–orbit interactions. Ligand field calculations show a remarkable agreement between the predicted energy levels and the transition energies observed in the near-IR luminescence spectrum. On warming, this crystal begins to show broad-band luminescence, which dominates above 70 K. The bromide host containing $Ti^{2+}$ shows broad-band near-IR luminescence at low temperature with a decay time of 750 μs. In both host lattices above 200 K nonradiative relaxation sets in. Luminescence decay times as a function of temperature are measured, which, in combination with the emission and absorption spectroscopy, leads to a detailed quantitative interpretation of the radiative and nonradiative relaxation mechanisms.

## I. Introduction

There are few well-characterized complexes of divalent titanium. The $Ti^{2+}$ ion has no aqueous chemistry, and very little information exists for this metal in oxidation states less than 3+. However, in the temperature range of the molten host lattices of this study, $MgCl_2$ (mp 714 °C) and $MgBr_2$ (mp 700 °C), the most stable oxidation state of titanium is 2+. By generating the $Ti^{2+}$ ions in situ in the melt, it is possible to stabilize the titanium ion in this oxidation state by subsequently growing a single crystal in a Bridgman furnace.[1]

From an optical spectroscopic viewpoint $Ti^{2+}$, having a $3d^2$ electron configuration, is very interesting, because it is the system treated in detail in almost every textbook on ligand field theory. Yet, experimental spectroscopic data are very scarce, and the textbook exercise is usually rather remote from physical reality. $Ti^{2+}$:$MgCl_2$ provides a beautiful example of a $d^2$ ion in an axial ligand field with a very large number of electronic states spectroscopically accessible. Figure 1 shows the Tanabe–Sugano diagram for an octahedral $d^2$ complex. The nature of the first excited state essentially determines the luminescence properties of a transition-metal complex. From Figure 1 we see that there is a crossover from a spin triplet at weak fields to a spin singlet at stronger fields. The latter derives from the same $(t_{2g})^2$ strong-field configuration as the ground state. Thus, providing that the ligand field is strong enough and that nonradiative relaxation cannot compete with the radiative mechanism, sharp-line luminescence should be observed from the excited singlet to the triplet ground state following photoexcitation into the higher energy spin-allowed triplets. In the 3d transition-metal series such intraconfigurational sharp luminescence transitions have mainly been observed in $d^3$ (doublet → quartet) systems. The majority of known $Cr^{3+}$ complexes exhibit sharp R-line luminescence in the red or near-infrared (near-IR) part of the spectrum. This is exemplified by the well-known R-line luminescence of $Cr^{3+}$ in $Al_2O_3$ (ruby). The isoelectronic $V^{2+}$[2] and $Mn^{4+}$[3] have also been shown to exhibit sharp luminescence in favorable host lattices. The minority of $Cr^{3+}$ compounds show $^4T_{2g} \rightarrow {}^4A_{2g}$ broad-band emission or, if they lie in the crossover region, simultaneous and temperature-dependent broad-band/sharp-band emission as found in $Cr^{3+}$:MgO,[4,5] alexandrite,[6] or the complex $Cr(urea)_6{}^{3+}$.[7]

Since $d^2$ and $d^3$ ions have very similar Tanabe–Sugano diagrams, a similar range of behavior is expected for $d^2$ systems, but so far these have remained largely unexplored. Sharp emission has been observed for the $d^2$ analogue of ruby ($V^{3+}$ in $Al_2O_3$). However, in this system, which exhibits two bands in the near-IR around 9950 $cm^{-1}$,[8] the emission intensity is very weak due to competing nonradiative processes even at low temperatures.[9,10] As far as octahedral $Ti^{2+}$ is concerned, the only report on luminescence to have appeared so far is a short note on the low-temperature spectrum of $Ti^{2+}$:$MgCl_2$.[11] It was shown in this study that the substitution of the impurity produced a large trigonal distortion that lifted a great deal of the 9-fold degeneracy of the $^3T_{1g}$ ($O_h$ notation) ground state of $Ti^{2+}$. This nicely illustrates the important difference between the $d^2$ and $d^3$ ground states. In $d^3$ systems, such as $Cr^{3+}$, no such first-order splitting occurs since the ground-state $^4A_{2g}$ is an orbital singlet.

We report here the results of a correlative study employing different experimental techniques on $Ti^{2+}$ in $MgCl_2$ and $MgBr_2$. Our goal is to explore the nature of the first excited states of these systems in the singlet/triplet spin crossover region and to study the effects of small changes in the chemical environment in going from chloride to bromide. Since virtually nothing is known about the excited states of $Ti^{2+}$ ions, an accurate determination of the equilibrium positions of the competing excited-state potential surfaces is highly desirable. A characterization of these properties is a prerequisite for understanding the potential photochemical and the photophysical properties of such transition-metal ions. In addition, 3d transition-metal ions that luminescence are likely to continue to play a role in the development of solid-state lasers, particularly in the near-IR.[12] A system such as $Ti^{2+}$:$MgCl_2$ in which the luminescence terminates in an electronically split ground state is interesting in view of its potential for semi-four-level laser operation.[13] Therefore a fundamental investigation of all the competing radiative and nonradiative processes is required. Our additional objective is to exactly determine the ground-state splitting of $Ti^{2+}$:$MgCl_2$ and reproduce it by simple theoretical

---

* Author to whom correspondence should be addressed.

[†] Institut für Anorganische Chemie der Universität Bern.

[‡] Institut de Chimie Inorganique, Université de Fribourg.

(1) Wilson, D. R.; Smith, W. E. *Inorg. Chem.* **1986**, *25*, 898.
(2) Sturge, M. D. *Phys. Rev.* **1965**, *140*, A880.
(3) Donegan, J. F.; Glynn, T. J.; Imbusch, G. F.; Remeika, J. P. *J. Lumin.* **1986**, *36*, 93.
(4) Parker, J. H., Jr.; Weinert, R. W.; Castle, J. G., Jr. In *Optical Properties of Ions in Crystals*; Crosswhite, H. M., Moos, H. W., Eds.; Wiley: New York, 1967; p 251.
(5) Castelli, F.; Forster, L. S. *Phys. Rev. B* **1975**, *11*, 920.
(6) Powell, R. C.; Xi, L.; Gang, X.; Quarles, G. T. *Phys. Rev. B* **1985**, *32*, 25788.
(7) Porter, G.; Schläfer, H. L. *Z. Phys. Chem.* (*Frankfurt*) **1963**, *37*, 109.
(8) Goldschmidt, Z.; Low, W.; Foguel, M. *Phys. Lett.* **1965**, *19*, 17.
(9) Riseberg, L. A.; Moos, H. W.; Pratlow, W. D. *IEEE J. Quant. Elec.* **1968**, *QE-4*, 609.
(10) Champagnon, B.; Duval, F. *J. Phys.* (*Paris*), *Lett.* **1977**, *38*, 299.
(11) Jacobsen, S. M.; Smith, W. E.; Reber, C.; Güdel, H. U. *J. Chem. Phys.* **1986**, *84*, 5205.
(12) Guenther, B. D.; Buser, R. G. *IEEE J. Quant. Elec.* **1982**, *QE-18*, 1179.
(13) Riseberg, L. A. In ref 23, pp 369–407.

0002-7863/88/1510-7610$01.50/0

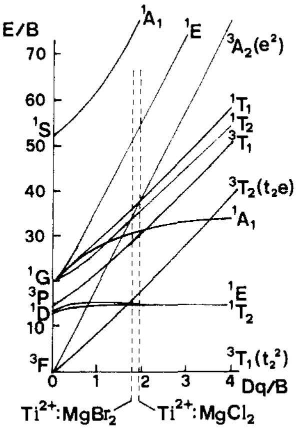

**Figure 1.** Tanabe–Sugano diagram for octahedral $d^2$. The broken lines indicate the approximate energies of the excited states for the ground-state equilibrium coordination.

model calculations. The energies of the ground-state levels in this system can be determined with an exceptional degree of accuracy, thus making it eminently suitable as a testing ground for the application of ligand field theory. We thus combine absorption and luminescence spectroscopy with lifetime measurements to draw conclusions about energy levels and radiative and nonradiative decay mechanisms for both systems.

## II. Experimental Section

**A. Synthesis.** Single crystals of $MgCl_2$ and $MgBr_2$ containing $Ti^{2+}$ were grown by the Bridgman technique using an in situ reaction to generate the titanium ions. The starting anhydrous magnesium halides (supplied by Norsk Hydro) were fused with a mixture of titanium metal powder (Johnson Matthey Specpure) and anhydrous $ZnCl_2$ or $ZnBr_2$ (BDH AnalaR) in a closed quartz tube that had been evacuated. A slight excess of titanium metal was used in order to ensure that all the $ZnCl_2$ was reduced in the reaction that produced the $Ti^{2+}$ ions. The tube was lowered through a steep temperature gradient in a Bridgman furnace at 800 °C (lowering rate = 1 mm/h). After the reaction it was noted that a small slug of zinc metal was produced below the resultant single crystals of $Ti^{2+}$ in magnesium halide. The titanium concentration was determined colorimetrically.

**B. Crystal Structures.** Magnesium chloride and magnesium bromide are layer lattices, each consisting of sheets of halide ions with the cations occupying every alternate layer, the layers themselves being held together by weak van der Waals forces. Crystals of magnesium chloride belong to the space group $D_{3d}^5$ ($R\bar{3}m$), where the cations occupy $D_{3d}$ sites that are only slightly trigonally distorted.[14] In magnesium bromide the cation site symmetry is also $D_{3d}$, the space group is $D_{3d}^3$ ($P\bar{3}m1$), and the only difference to the chloride is in the stacking arrangement of layers.[15] In the doped crystals we assume that the $Ti^{2+}$ ions isomorphously substitute for the $Mg^{2+}$ ions. It is obvious from the rather large difference in ionic radii between the host and the dopant ions ($Ti^{2+}$ = 0.94 Å, $Mg^{2+}$ = 0.66 Å)[16] that a considerable amount of compensating distortion must occur in the lattice around the impurity site. We can envisage that this will lead to an increase in the ligand field strength around an impurity ion (i.e., an increase in the ligand field parameter $Dq$) compared to pure $TiCl_2$ or $TiBr_2$ and, because of the nephelauxetic effect, the formation of rather more covalent Ti–Cl and Ti–Br bonds (i.e., a reduction of the Racah parameters). As we shall see in section IV, this overall increase in the ratio $Dq/B$ makes sharp-line luminescence more favorable.

Because of the nature of the layer structure, the crystals cleave readily perpendicular to the $c$ axis, allowing axial spectra to be obtained easily. For the polarized absorption spectra of 5% $Ti^{2+}$:$MgCl_2$, a crystal was carefully cut and polished parallel to the $c$ axis, thus allowing $\sigma(E \perp c)$ and $\pi(E \parallel c)$ spectra to be obtained.

**C. Spectroscopic Measurements.** Overall near-IR-vis absorption spectra were obtained on a Beckman Acta IV spectrometer equipped with an Air Products Displex closed-cycle cryogenic refrigerator for temperatures down to 10 K. Luminescence spectra were obtained as follows. Axially oriented samples were mounted in quartz flow tubes and cooled with helium gas. The luminescence was excited with a Varian VIX 150 UV xenon lamp, dispersed by a $^3/_4$-m Spex 1702 monochromator and detected with either a cooled (77 K) PbS cell (Santa Barbara Research) or a cooled (77 K) germanium photodetector (Applied Detector Corp., 403L). The signal was recorded by using a PAR 186A lock-in amplifier in combination with a tuning-fork chopper (Bulova) to improve the signal to noise ratio. Data acquisition and monochromator control were performed by a Tektronix 4052A microcomputer system.

**D. Luminescence Decay Curves.** The 647.1-nm line of a krypton ion laser (Coherent CR 500K) was used as an excitation source. Pulses of laser light were obtained with an external Bragg cell (Coherent 305). The luminescence was detected through a cutoff filter (Schott RG 1000) with a germanium photodiode (Rofin Model 7462, operating at room temperature) using a preamplifier (PAR 115), and the decay was measured with a boxcar integrator (PAR 162 with PAR 164 gated integrator) interfaced with the Tektronix 4052A. For lifetimes longer than 20 ms a cooled (77 K) high-speed germanium photodetector (Applied Detector Corp., 403 HS) was used in conjunction with a Tektronix digital oscilliscope (2430A) with storage and averaging facilities. We consider these measurements more accurate than those previously reported for this system,[17] in which the very long decay times were measured by photographic recording of an oscilliscope screen (Tektronix 5103N) after a single laser pulse. The difference between the two sets of measurements is within 10%.

**E. Ligand Field Calculation.** Here we present an outline of the method of computation used in the full ligand field calculation (calculation b) presented in section IVA. A more detailed account of the principle is given in ref 18.

For our computation we are interested in all the states within the $d^2$ ligand field manifold. We take the threefold axis as the axis of quantization (trigonal symmetry) and the following symmetry-adapted combinations of real d orbitals as basis functions:

$$\Phi_1(a_1) = d_{z^2}$$

$$\Phi_2(1e\theta) = \sqrt{(2/3)}d_{x^2-y^2} - \sqrt{(1/3)}d_{xz}$$

$$\Phi_3(1e\epsilon) = \sqrt{(2/3)}d_{xy} + \sqrt{(1/3)}d_{yz}$$

$$\Phi_4(2e\theta) = \sqrt{(1/3)}d_{x^2-y^2} + \sqrt{(2/3)}d_{xz}$$

$$\Phi_5(2e\epsilon) = \sqrt{(1/3)}d_{xy} - \sqrt{(2/3)}d_{yz} \qquad (1)$$

Using a computer program we generated the 45 determinantals corresponding to all possible accommodations of two electrons within all ligand field configurations. The full configurational interaction matrix was then calculated within these determinantals for the Hamiltonian:

$$H = V_{LF} + \sum_{i<j} e^2/r_{ij} + \sum_{i} \zeta \mathbf{l}_i \cdot \mathbf{s}_i \qquad (2)$$

where the second term on the right-hand side describes the electrostatic repulsion of electrons and the third term represents the spin–orbit interaction. The nonvanishing one-electron matrix elements of $V_{LF}$ for trigonal symmetry are

$$\langle 1e|V_{LF}|1e\rangle = -4Dq + D_\sigma + (2/3)D_\tau$$

$$\langle a_1|V_{LF}|a_1\rangle = -4Dq - 2D_\sigma + 4D_\tau$$

$$\langle 2e|V_{LF}|2e\rangle = 6D_q + (7/3)D_\tau$$

$$\langle 1e|V_{LF}|2e\rangle = \sqrt{2}D_\sigma + [(5\sqrt{2})/3]D_\tau \qquad (3)$$

Using eq 1, one can easily evaluate the electrostatic matrix elements in terms of the Racah parameters $B$ and $C$ and the spin–orbit coupling matrix elements in terms of $\zeta$.

The magnetic dipole transition moments used in the discussion of relative emission lifetimes and intensities were obtained in a similar way by calculation of the following matrix elements:

$$M_{ij} = \langle i|k\mathbf{l} + 2\mathbf{s}|j\rangle \qquad (4)$$

where $i$ and $j$ are labels for the wave functions obtained after diagonalization of $H$, and $k$ is an orbital reduction factor.

## III. Results

Axial absorption spectra of $Ti^{2+}$ in $MgCl_2$ with varying concentrations of dopant have been reported.[1] Figure 2 shows the polarized absorption at 10 K of a crystal containing 5% $Ti^{2+}$. The

---

(14) Wycoff, R. W. G. *Crystal Structures*, 2nd ed.; Interscience: New York, 1965; Vol. 1, p 270.

(15) Anderson, A.; Lo, Y. W. *Spectrosc. Lett.* **1981**, *14*, 603.

(16) *Handbook of Chemistry and Physics*; CRC: Boca Raton, FL, 1982–1983; p F-179.

(17) Jacobsen, S. M.; Güdel, H. U. Proceedings of the 1987 International Conference on Luminescence, Peking, China (to be published in *J. Lumin.*).

(18) Daul, C. A.; Goursot, A. *Int. J. Quant. Chem.* **1986**, *26* 779.

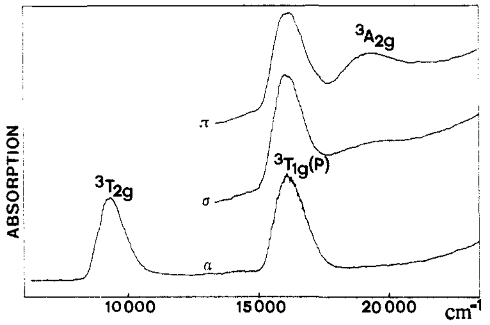

Figure 2. Polarized near-IR–vis absorption spectra of $Ti^{2+}:MgCl_2$ at 10 K. $\pi(E \parallel c)$, $\sigma(E \perp c)$, $\alpha$ = axial.

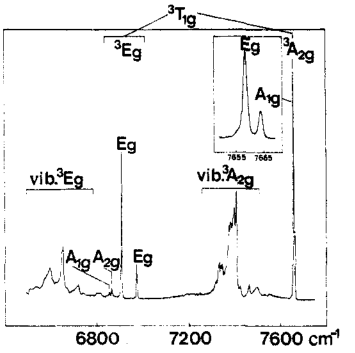

Figure 3. Unpolarized axial near-IR emission spectrum of 0.1% $Ti^{2+}:MgCl_2$ at 10 K. The insert shows the high-resolution spectrum of the $^3A_{2g}$ ($D_{3d}$ notation) origins.

broad absorption bands at 9260 and 16 130 cm$^{-1}$ are the two spin-allowed ligand field bands $^3T_{1g} \rightarrow {}^3T_{2g}$, $^3T_{1g}$ (P) ($O_h$ notation) expected for an octahedral $d^2$ ion. Comparison of the axial ($\alpha$) with the $\sigma$ and $\pi$ spectra shows that an additional broad band centered at 19 340 cm$^{-1}$ appears only in $\pi$-polarization. Its assignment as $^3A_{2g}$ is discussed in section IVA. The 10 K axial absorption spectrum of $Ti^{2+}$ in $MgBr_2$, not shown here, is similar to that of the chloride, with the ligand field bands $^3T_{1g} \rightarrow {}^3T_{2g}$, $^3T_{1g}$ (P) at 8220 and 15 040 cm$^{-1}$, respectively.

Figure 3 shows the 10 K near-IR luminescence spectrum (axial) of a crystal of $MgCl_2$ containing 0.1% $Ti^{2+}$. All the bands in this spectrum are due to transitions from the $^1E_g$ ($D_{3d}$ notation) excited state to the trigonally split $^3T_{1g}$ ground state of $Ti^{2+}$. Numerical values of the electronic origin transitions are listed in Table I. Assignments and a quantitative analysis of energy differences are given in section IVA and Table I.

The temperature dependence of the $Ti^{2+}:MgCl_2$ luminescence is shown in Figure 4. Between 19 and 94 K the contribution from the sharp-line component decreases rapidly, and there is a concomitant rise in a broad emission band centered around 6400 cm$^{-1}$. The ratio of broad-band to sharp-line emission intensity was determined for various temperatures. It is plotted on a logarithmic scale as a function of $1/T$ in Figure 6 and will be analyzed in section IVB.

The 20 K luminescence from a crystal of 5% $Ti^{2+}:MgBr_2$ is shown in the lowest trace of Figure 3. This broad-band emission at low temperatures is in marked contrast to the highly resolved chloride low-temperature emission. We also note that this emission band is significantly narrower than the broad-band emission of $Ti^{2+}:MgCl_2$ observed at 170 K. The large width in the chloride is mainly the result of the large (~750 cm$^{-1}$) trigonal splitting of the $^3T_{1g}$ ground state. The bromide is much closer to octahedral, and the analysis will be carried out assuming $O_h$ symmetry.

Luminescence decay curves were measured for both systems as a function of temperature. With the exception of a small contribution from a fast-decaying component in the chloride, they were found to be single exponentials and lifetimes ($\tau$) could thus be determined. Figure 5 shows the temperature dependence of $\tau$ for $Ti^{2+}:MgCl_2$ between 10 K and room temperature. The sharp drop of $\tau$ by an order of magnitude between 40 K and 100 K parallels the observed decrease of sharp-line to broad-band intensity in the same temperature interval. It is not accompanied by a corresponding decrease in the total emission intensity within the experimental error of the measurements (±10%) as is illustrated by the observed emission intensity versus temperature, which

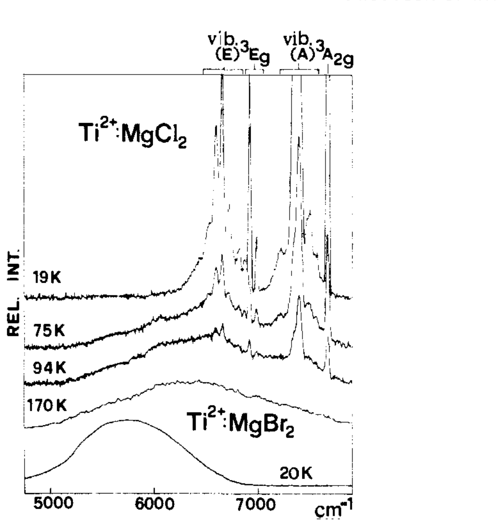

Figure 4. Temperature dependence of the 0.1% $Ti^{2+}:MgCl_2$ emission along with the low-temperature emission from $Ti^{2+}:MgBr_2$.

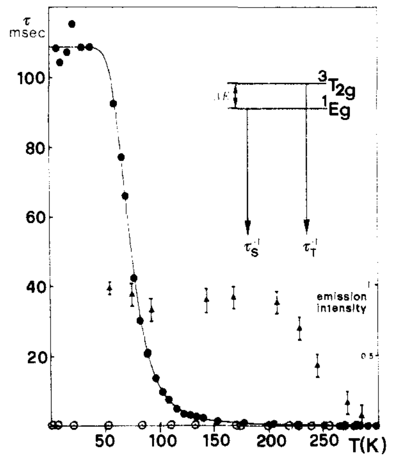

Figure 5. Near-IR luminescence decay times versus temperature for $Ti^{2+}$. The solid circles show the experimental values for $Ti^{2+}:MgCl_2$, and the solid line is a fit to the two-level emitting model shown in the insert, which is further explained in the text (see eq 6 in section IVB). The open circles show the lifetimes of $Ti^{2+}:MgBr_2$. Also included is the emission intensity versus temperature for $Ti^{2+}:MgCl_2$ (triangles with estimated error bars).

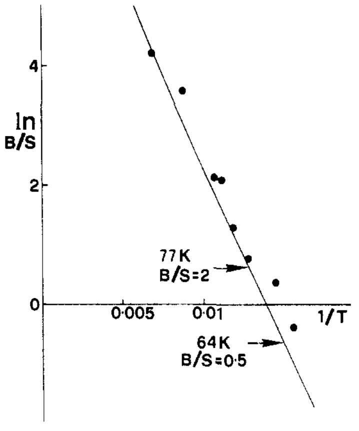

Figure 6. Broad-band to sharp-line intensity ratios plotted on a logarithmic scale versus $1/T$ for $Ti^{2+}:MgCl_2$. The solid circles are measured ratios. The solid line is not a fit to these ratios but is generated from the lifetime analysis by eq 7, with parameter values in Table II.

**Table I.** Calculated and Observed Energy Levels (cm$^{-1}$) for the Ground-State Equilibrium Geometry of Ti$^{2+}$:MgCl$_2$ along with the Relevant parameter Values

| | | | | | | obsd | |
|---|---|---|---|---|---|---|---|
| | $O_h$ | $D_{3d}$ | spinors | calcd$^a$ | calcd$^b$ | emission | absorption |
| $(t_{2g})^2$ | $^3T_{1g}$ | $^3A_{2g}$ | $A_{1g}$ | 0 | 0 | 0 | |
| | | | $E_g$ | 3.6 | 4.26 | 4.7 | |
| | | $^3E_g$ | $E_g$ | 689.8 | 691.5 | 689.4 | |
| | | | $E_g$ | 750.0 | 752.2 | 757.0 | |
| | | | $A_{2g}$ | 801.8 | 801.0 | 799.5 | |
| | | | $A_{1g}$ | 809.6 | 811.6 | 810.4 | |
| $(t_{2g})^2$ | $^1T_{2g}$ | $^1E_g$ | $E_g$ | | 7664.6 | 7664.6 | |
| $(t_{2g})^2$ | $^1E_g$ | $^1E_g$ | $E_g$ | | 8202.6 | | |
| | | $^1A_{1g}$ | $A_{1g}$ | | 8232.2 | | |
| $(t_{2g}e_g)$ | $^3T_{2g}$ | $^3A_{1g}$ | $A_{2g}$ | | 9216 | | |
| | | | $E_g$ | | 9232 | | |
| | | $^3E_g$ | $A_{1g}$ | | 9310 | | 9260 |
| | | | $A_{2g}$ | | 9316 | | |
| | | | $E_g$ | | 9326 | | |
| | | | $E_g$ | | 9333 | | |
| $(t_{2g})^2$ | $^1A_{1g}$ | $^1A_{1g}$ | $A_{1g}$ | | 15935 | | |
| $(t_{2g}e_g)$ | $^3T_{1g}$ | $^3E_g$ | $A_{2g}$ | | 16037 | | |
| | | | $E_g$ | | 16069 | | |
| | | | $A_{1g}$ | | 16106 | | 16130 |
| | | | $E_g$ | | 16111 | | |
| | | $^3A_{2g}$ | $E_g$ | | 16306 | | |
| | | | $A_{1g}$ | | 16314 | | |
| $(t_{2g}e_g)$ | $^1T_{2g}$ | $^1A_{1g}$ | $A_{1g}$ | | 17612 | | |
| | | $^1E_g$ | $E_g$ | | 17916 | | |
| $(e_g)^2$ | $^3A_{2g}$ | $^3A_{2g}$ | $E_g$ | | 19290 | | 19340 |
| | | | $A_{1g}$ | | 19292 | | |
| $(t_{2g}e_g)$ | $^1T_{1g}$ | $^1A_{2g}$ | $A_{2g}$ | | 19518 | | |
| | | $^1E_g$ | $E_g$ | | 19573 | | |
| $(e_g)^2$ | $^1E_g$ | $^1E_g$ | $E_g$ | | 27389 | | |
| $(e_g)^2$ | $^1A_{1g}$ | $^1A_{1g}$ | $A_{1g}$ | | 38225 | | |

[a] Effective Hamiltonian for $^3T_{1g}$ only, $\zeta = 112$ cm$^{-1}$, $V_{\rm trig} = -246$ cm$^{-1}$. [b] Full ligand field calculation: $Dq = 1018$ cm$^{-1}$, $B = 527$ cm$^{-1}$, $C = 1983$ cm$^{-1}$, $D_\sigma = 281$ cm$^{-1}$, $D_\tau = -142$ cm$^{-1}$, $\zeta = 93$ cm$^{-1}$ $(C/B = 3.76)$ $(Dq/B = 1.93)$.

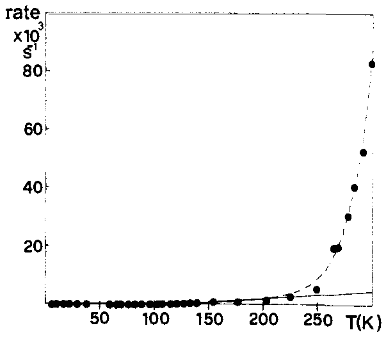

**Figure 7.** Ti$^{2+}$:MgCl$_2$ near-IR decay rate $(1/\tau)$ versus temperature. Solid circles show experimental values. The solid line shows the fit to the purely radiative model discussed in section IVB and given by eq 6. The dashed line includes the nonradiative model discussed in section IVC and given by eq 15b, with parameter values in Table II.

is included in Figure 5 for Ti$^{2+}$:MgCl$_2$. The temperature dependence of $\tau$ for Ti$^{2+}$:MgBr$_2$ is also included in Figure 5, illustrating the marked difference in time regimes between chloride and bromide emissions.

A second drop of luminescence lifetimes, this time accompanied by an analogous drop in the total emission intensity, occurs between 200 and 300 K for both systems. This is better visualized by a plot of the decay rate $(1/\tau)$ versus temperature, as shown for the chloride in Figure 7 and for the bromide in Figure 8. These phenomena will be analyzed in section IVC.

Below 40 K Ti$^{2+}$:MgCl$_2$ shows some highly unusual luminescence properties, which we briefly summarize here but which will be discussed in detail in a future article. They do not affect the conclusions reached in the present article. Besides the near-IR emission reported here Ti$^{2+}$:MgCl$_2$ exhibits a broad-band emission centered at 13 340 cm$^{-1}$ at low temperatures. Its intensity and lifetime ($\tau = 20$ μs at 10 K) abruptly drop to zero between 30 and 40 K. In the same temperature range the near-IR emission loses 33% of its intensity when excited in the visible but stays constant when excited in the near-IR via the $^3T_{1g} \rightarrow {}^3T_{2g}$ absorption. The 13 340-cm$^{-1}$ emission is ascribed to a $^3T_{1g}$ (P) $\rightarrow {}^3T_{1g}$ transition.

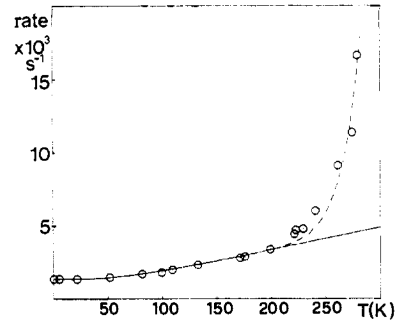

**Figure 8.** As for Figure 7, but for Ti$^{2+}$:MgBr$_2$. The solid line is a fit to eq 5 and the dashed line to eq 15a, with parameter values in Table II.

## IV. Discussion

**A. Energy Splittings and Intensity Mechanisms.** In this discussion we will use octahedral notation, unless otherwise stated, for the designation of states.

As shown in section III, the assignment of the structureless absorption bands observed in both host lattices to the spin-allowed ligand field transitions is straightforward. In Ti$^{2+}$:MgCl$_2$ the third ligand field transition $^3T_{1g} \rightarrow {}^3A_{2g}$ is clearly observable in $\pi$-polarization. This is a two-electron excitation in the strong-field approximation and, as such, is expected to be weak as observed. Its energy separation from $^3T_{1g} \rightarrow {}^3T_{2g}$ is 10 080 cm$^{-1}$, which corresponds to $10Dq$ in ligand field theory. From its observed polarization behavior (Figure 2) it follows immediately that the transition occurs by an electric dipole (ED) mechanism, and from the predominant $\pi$-polarization we conclude that an $a_{2u}$ ($D_{3d}$ notation) vibration acts as the principle enabling mode in the vibronic intensity gaining mechanism.

We note that there is a complete lack of any sharp absorption bands in the low-energy near-IR region. No information about singlet states is thus obtained from the absorption spectra. In contrast, the luminescence spectra are an invaluable source of information about energy splittings and intensity mechanisms. In the bromide at all temperatures and in the chloride above 100 K we have the "normal" situation of a broad emission band Stokes shifted from the first absorption band, corresponding to the transitions $^3T_{1g} \leftrightarrow {}^3T_{2g}$. The Stokes shift is the result of a displacement of the excited-state potential energy surface with respect to the ground-state potential along a displacement coordinate. This will be quantitatively analyzed in section IVC.

At temperatures below 100 K the Ti$^{2+}$:MgCl$_2$ emission spectrum completely changes its character by developing a different shape and a great deal of fine structure. This change of character is obviously the result of the population of a different emitting state. This is most easily discussed by using the Tanabe–Sugano diagram in Figure 1. Depending on the $Dq/B$ ratio the emitting state is either $^3T_{2g}$ (weak field) or $^1T_{2g}$ (strong field). In our host lattices we are close to the crossover of these two states. In the bromide host $^3T_{2g}$ remains the emitting state down to the lowest temperatures, whereas in the chloride a $^1E_g$ ($D_{3d}$ notation) component becomes the dominant emitting state below 70 K. The sharpness of the low-temperature (LT) emission bands in Ti$^{2+}$:MgCl$_2$ is a direct result of their intraconfigurational nature. Both the ground and singlet excited states derive from the $(t_{2g})^2$ strong-field electron configuration and thus have potential energy surfaces with very similar equilibrium geometries. The broken vertical lines in Figure 1 indicate the relevant positions in the Tanabe–Sugano diagram for the ground state geometry. It is important to note that this diagram is inadequate for a comprehensive discussion of the luminescence properties. The displacement of the competing emission states with respect to some distortion coordinate will have to be taken into account explicitly. This results in the representations shown in Figure 9. The

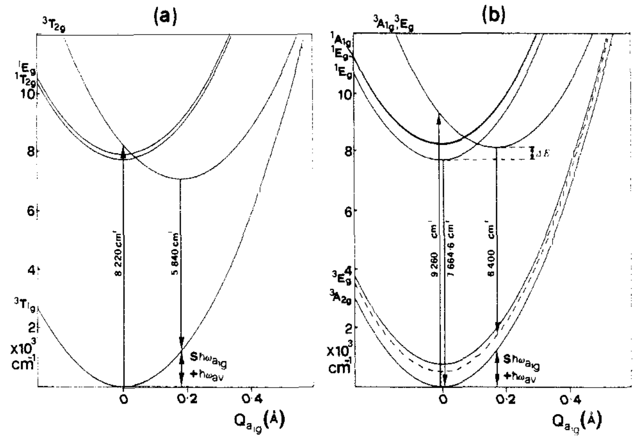

**Figure 9.** Configurational coordinate diagrams for (a) $Ti^{2+}$:$MgBr_2$ and (b) $Ti^{2+}$:$MgCl_2$. For $Ti^{2+}$:$MgBr_2$ $O_h$ notation is used for the designation of states. The vertical arrows indicate the observed absorption and luminescence transitions. For $Ti^{2+}$:$MgCl_2$ $D_{3d}$ notation is used but spin–orbit coupling is neglected. Also neglected is the trigonal splitting of the triplet excited state.

procedure is described in section IVC.

Here we are interested in an assignment of the sharp-line emission in Figure 2. A brief account of this has been given elsewhere,[11] and the emitting state has been unambiguously assigned as $^1E_g$ ($D_{3d}$) on the basis of the polarization behavior. The six exceedingly sharp lines are all assigned as pure electronic transitions to six spinor components of the ground state. They are designated in $D_{3d}$ notation in Figure 2. The electronic lines are accompanied by the somewhat broader vibronic sidebands vib $^3A_{2g}$ and vib $^3E_g$. From the observed intensity distribution it is clear that the dominant sidebands are vibronic origins. In contrast to the electronic origins, which must have magnetic-dipole (MD) character, their intensity is ED. We estimate an ED/MD ratio of 5/1 for the total emission intensity. The energy displacement of the sidebands from the origins ranges from 165 to 320 cm$^{-1}$. The likely enabling vibrations are $e_u$ and $a_{2u}$ lattice modes, with the actual frequencies and intensities being determined by the quasi-localized modes selected by the $Ti^{2+}$ impurity.

Since for $Ti^{2+}$:$MgCl_2$ we now have a large number of very accurate energy levels, it is tempting to fit them with a theoretical model. We performed two such calculations:

(a) The first calculation was a calculation of the $^3T_{1g}$ ground state splitting using an appropriate effective Hamiltonian. The method is outlined in ref 19. There are only two effective adjustable parameters in this model, one for the trigonal ligand field ($V_{trig}$) and one for the spin–orbit coupling ($\zeta$). The number of observed energy differences is five.

(b) The second calculation was a complete ligand field calculation of the $d^2$ electron configuration including trigonal field and spin–orbit interactions, as outlined in section IIE. This is a six-parameter model, and the number of observed energy differences (from absorption and luminescence) is nine.

The results of both calculations are compared with the experimental energies in Table I. The agreement is remarkable, in particular for the simple two-parameter model a, which reproduces the five energy intervals almost to the dot. This excellent agreement is undoubtedly the result of the energetic isolation of the $^3T_{1g}$ ground state, which reduces higher order mixings with other states to the point that they become negligible. The $^3T_{1g}$ ground state thus exhibits practically pure first-order behavior. This is a very rare example of such behavior. When applied to excited orbital triplets a Hamiltonian of type a is never as successful as here because of second-order mixing with nearby excited states. For other ions with orbital triplet ground states the energy splitting is usually spectroscopically unaccessible.

The complete ligand field calculation b provides us with a reliable set of parameters (Table I). It reveals that the trigonal splitting, which is of the order of 750 cm$^{-1}$ in the $^3T_{1g}$ ground state, is expected to be of the order of 100 cm$^{-1}$ in the $^3T_{2g}$ excited state. It also shows that the lowest excited state $^1E_g$ ($D_{3d}$) is separated by more than 500 cm$^{-1}$ from the next higher singlet state. This is in good accordance with our inability to detect any hot sharp-line luminescence. The value of the spin–orbit coupling parameter is $\zeta$ = 93 cm$^{-1}$, compared with $\zeta$ = 123 cm$^{-1}$ for the free ion.[22]

For $Ti^{2+}$:$MgBr_2$ we only have two absorption band positions for an estimate of ligand field parameters. Working in the octahedral approximation and taking $C/B$ = 4.19 as in the free ion, we obtain $B$ = 514 cm$^{-1}$ and $Dq$ = 910 cm$^{-1}$. As expected from their relative positions in the spctrochemical series, $Dq$ for the chloride (1018 cm$^{-1}$) is greater than for the bromide. The Racah parameter $B$ is reduced from 527 cm$^{-1}$ in the chloride to 514 cm$^{-1}$ in the bromide, as expected from their positions in the nephelauxetic series.

There is no indication for the presence of a Jahn–Teller effect in the $^3T_{1g}$ ground state of $Ti^{2+}$:$MgCl_2$, as might be observed through a Ham quenching of the trigonal and spin–orbit splittings. In $V^{3+}$:$Al_2O_3$ a Jahn–Teller distortion was found in the $^3T_{2g}$ excited state, but none in the $^3T_{1g}$ ground state.[20] The situation may be quite similar for the present systems. Since $^3T_{1g}$ derives from the $(t_{2g})^2$ electron configuration there is no first-order coupling to $e_g$ modes. In addition, the large trigonal ligand field in the chloride host lattice is likely to quench a small Jahn–Teller coupling. In the excited $^3T_{2g}$ state, which derives from the ($t_{2g}$ $e_g$) electron configuration, the situation may be quite different with an acutal Jahn–Teller distortion, but since the $^3T_{2g} \leftrightarrow {}^3T_{1g}$ transitions show no fine structure we have no direct spectroscopic evidence for it.

**B. Radiative Excited-State Decay Mechanisms.** In this discussion we make the assumption that the excited-state decay up to 200 K is purely radiative for both lattices. This is based on the observation that total luminescence intensities remain constant within experimental accuracy between 40 and 200 K. the anomalous behavior of $Ti^{2+}$:$MgCl_2$ when excited in the visible below 40 K, which was briefly mentioned in section III, does not affect this discussion. We are only concerned here with the processes that take place once the system has relaxed into the lowest energy excited states.

The behavior of the $Ti^{2+}$ luminescence in the two host lattices is distinctly different between 10 and 200 K, and we can immediately draw the following conclusions. The $Ti^{2+}$:$MgBr_2$ emission is a $^3T_{2g}$ emission at all temperatures. The observed gradual increase in the decay rate with increasing temperature results from the vibronic mechanism, which increases the overall transition probability at high temperatures. In $Ti^{2+}$:$MgCl_2$, on the other hand, the principal temperature effect, namely, the drop of $\tau$ by an order or magnitude between 40 and 100 K, is the result of a singlet/triplet spin crossover of the emitting state. In the following we use simple models for a quantitative interpretation of the data.

We discuss the bromide data first. The temperature dependence of the vibronic transition probability can be described by the well-known coth ($\hbar\omega_{av}/2kT$) function, where $\hbar\omega_{av}$ represents a properly weighted average of enabling vibrational frequencies. Hence the $^3T_{2g} \rightarrow {}^3T_{1g}$ luminescence decay rate is given by

$$\tau^{-1} = \tau_T^{-1} \coth (\hbar\omega_{av}/2kT) \qquad (5)$$

where $\tau_T$ is the decay time at 0 K. A least-squares fit of eq 5 to the data in Figure 8 yielded the parameter values $\tau_T$ = 750 $\mu$s and $\hbar\omega_{av}$ = 119 cm$^{-1}$. The experimental behavior up to 200 K is well represented by eq 5, and the result of the fit is shown as a full line in Figure 8.

For $Ti^{2+}$:$MgCl_2$ we use the following simplified model. Two excited states with an energy separation of $\Delta E$ contribute to the

---

(19) Sugano, S.; Tanabe, Y.; Kamimura, H. *Multiplets of Transition Metal Ions in Crystals*; Academic: New York/London, 1970; see problem 7.5, p 170.

(20) Scott, W. C.; Sturge, M. D. *Phys. Rev.* **1966**, *146*, 262.

(21) Imbusch, G. F. In *Luminescence Spectroscopy*, Lumb, M., Ed.; Academic: New York, 1978.

(22) Figgis, B. *Introduction of Ligand Fields*; Interscience: New York, 1966; p 60.

**Table II.** Parameter Values for Radiative and Nonradiative Decay Models[a]

| parameter | $Ti^{2+}$:$MgBr_2$ | $Ti^{2+}$:$MgCl_2$ |
|---|---|---|
| $\tau_S$, ms | | 109 |
| $\tau_T$, μs | 750 | 189 |
| $\Delta E(^1E_g-^3T_{2g})$, cm$^{-1}$ | | 401 |
| $\hbar\omega_{av}$, cm$^{-1}$ | 119 | 180 |
| $\hbar\omega_{a_{1g}}$, cm$^{-1}$ | 165 | 260 |
| Stokes shift, cm$^{-1}$ | 2380 | 2360 |
| $S$(Huang–Rhys) | 6.50 | 3.85 |
| $\Delta E(^3T_{1g}-^3T_{2g})$, cm$^{-1}$ | 7030 | 8330 |
| $P$ | 43 | 32 |
| $\tau_{NR}^{-1}(0)$ | $2.7 \times 10^{-3}$ | 59.6 |
| $\Delta Q_{a_{1g}}$, Å | 0.18 | 0.17 |

[a] See sections IVB and IVC for explanation of parameters.

emission: the lowest energy $^1E_g$ state ($D_{3d}$ notation) and the $^3T_{2g}$ ($O_h$ notation) state. We thus neglect any splitting of $^3T_{2g}$ due to the trigonal ligand field and spin–orbit coupling. There are good reasons for doing so: The ligand field calculation indicates that the $^3T_{2g}$ splitting is of the order of 100 cm$^{-1}$, which may be further reduced by the presence of a Ham effect. We can safely ignore the other singlet states ($^1A_{1g}$, $^1E_g$ ($D_{3d}$ notation)) because they are separated from the lowest energy $^1E_g$ state by at least 500 cm$^{-1}$, and in addition their small rates would make a negligible contribution. The total decay rate can then be expressed as

$$\tau^{-1} = P_S\tau_S^{-1} + P_T\tau_T^{-1} \coth(\hbar\omega_{av}/2kT) \tag{6}$$

$$P_S = 2/Z$$

$$P_T = 9\exp(-\Delta E/kT)/Z$$

$$Z = 2 + 9\exp(-\Delta E/kT)$$

$P_S$ and $P_T$ are the singlet and triplet Boltzmann populations, respectively, and $\tau_S$ and $\tau_T$ are their intrinsic lifetimes. Also included is the coth factor pertaining to the high-temperature broad-band emission as in the bromide. The result of a least-squares fit of eq 6 to the lifetime data with $\tau_S$, $\tau_T$, $\Delta E$, and $\hbar\omega_{av}$ as adjustable parameters is shown by the solid lines in Figures 5 and 7. The experimental behavior is well described by the model and the corresponding parameter values are given in Table II.

As a separate check on the validity of the lifetime analysis, we calculated the expected ratio of broad-band to sharp-band emission intensity, which is given by the following equation:

$$B/S = \frac{9\tau_S \exp(-\Delta E/kT)\coth(\hbar\omega_{av}/2kT)}{2\tau_T} \tag{7}$$

The values of $\tau_S$, $\tau_T$, $\Delta E$, and $\hbar\omega_{av}$ were taken from the lifetime analysis. The result is shown and compared to the experimental ratios in Figure 6. Considering the fact that no parameter was fitted to obtain this correlation, the agreement is excellent, thus providing convincing support for our model and the parameter values. We draw attention to the dramatic change in $B/S$ ratios across a very small temperature range. At 64 K the ratio $B/S$ is 0.5, but at 77 K, this ratio is 2. This is a consequence of the large difference between the values $\tau_S$ and $\tau_T$ as well as the higher degeneracy of the triplet.

We note the unusually long singlet lifetime $\tau_S$ = 109 ms, which is more than an order of magnitude longer than for the emission in ruby at low temperatures. It is a result of the extreme forbiddenness of the sharp luminescence transitions. From the $\tau_S$ value and intensity ratios observed in the low-temperature luminescence spectrum we can obtain an estimate of the oscillator strength of the purely electronic $^3A_{2g} \leftrightarrow {}^1E_g$ ($D_{3d}$ notation) MD transition. The formula connecting radiative lifetime ($\tau_R$) and oscillator strength ($f$) for a given magnetic dipole electronic transition is the following:[21]

$$f(\mathrm{MD})\tau_R = 1.5 \times 10^4\left(\frac{\lambda_0^2}{n^3}\right) \quad \text{(SI units)} \tag{8}$$

where $\lambda_0$ is the wavelength of the transition and $n$ the refractive index of the crystal. Using the values $\lambda_0$ = 1300 nm and $n$ = 1.6 and estimating that the $^1E_g \rightarrow {}^3A_{2g}$ origins account for 6.5% of the total luminescence intensity, we obtain $f(\mathrm{MD}) = 4 \times 10^{-9}$ for this transition. This very small number explains why we were unable to detect this transition in absorption even in crystals containing 5% $Ti^{2+}$.

A comparison of $\tau_S$ = 109 ms and $\tau_T$ = 189 μs for $Ti^{2+}$:$MgCl_2$ is also interesting. They differ by a factor of 580 and we can rationalize this in the following way. Spin-forbidden transitions gain intensity via spin–orbit mixing with close-lying spin-allowed transitions. For the $^1E_g$ emission we know from experiment that the ratio of ED/MD intensity is 5/1. We assume the same ratio for the $^3T_{2g}$ emission; i.e., we assume that the efficiency of the vibronic intensity gaining mechanism is the same for both emissions. With this assumption we can estimate the $\tau_T/\tau_S$ ratio, because we can calculate it for the MD part of the transition.

Simply considering the first-order mixing of $^1E_g$ with the relevant spinor components of $^3T_{2g}$ under spin-orbit coupling, we obtain

$$\tau_T/\tau_S = (\zeta/\Delta)^2 \tag{9}$$

where $\zeta$ is the one-electron spin–orbit coupling parameter and $\Delta$ is the singlet–triplet energy separation for the singlet equilibrium geometry. Using the value $\zeta$ = 93 cm$^{-1}$ obtained from the full ligand field calculation and obtaining $\Delta$ by subtracting 7664.6 cm$^{-1}$ (the singlet–ground state energy separation) from 9260 cm$^{-1}$, the absorption maximum of $^3T_{2g}$ (see Table I), we obtain $3.4 \times 10^{-3}$ for $\tau_T/\tau_S$. This compares very favorably with the experimental value of $1.7 \times 10^{-3}$.

In a more accurate estimate we used the wave functions obtained in the full ligand field calculation to evaluate matrix elements of the magnetic moment operator, as outlined in section IIE and thus obtain oscillator strengths. The $\tau_T/\tau_S$ ratio calculated in this way is $1.5 \times 10^{-3}$, very close to the experimental value. In view of the fact that most of the intensity is ED, this agreement is rather surprising. It shows that our assumption of equal vibronic promoting efficiencies for the two transitions must be very good. We note that since $\zeta$ enters eq 9 as a quadratic term, its magnitude greatly influences the lifetime $\tau_S$. Values of $\zeta$ for the free ions $Ti^{2+}$, $V^{3+}$, $Cr^{3+}$, and $Mn^{4+}$ (i.e., those ions for which spin-forbidden sharp luminescence is observed) are tabulated in ref 22 as 123, 170, 275, and 415 cm$^{-1}$, respectively. $\zeta$ for $Ti^{2+}$ is by far the smallest in this series, and this helps to explain the unusually long lifetime $\tau_S$ found for $Ti^{2+}$:$MgCl_2$ in this study.

$\tau_T$ is larger in the bromide than in the chloride by a factor of 4. This difference cannot be due to the MD part of the intensity, because the electronic wave functions are rather similar in the chloride and bromide. We therefore have to ascribe it to a more efficient vibronic intensity gaining mechanism in the bromide. The effective, average frequencies for the enabling modes obtained in our fits—180 and 119 cm$^{-1}$ for the chloride and bromide, respectively—appear to be reasonable. In particular, their ratio of 0.66 lies well within the range of vibrational frequency ratios found between chloride and bromide lattices.

**C. Nonradiative Excited-State Decay Mechanisms.** The drop of luminescence lifetimes accompanied by a drop of total intensity that is observed for both host lattices between 200 and 300 K is clear evidence for the onset of nonradiative decay processes. The literature coverage of radiationless excited-state decay in the solid state is extensive.[23] Numerous physical processes can contribute to an overall nonradiative decay of luminescence. The most likely mechanism in our case is the so-called multiphonon relaxation, in which the electronic excitation energy is transformed into vibrational energy and thus finally into heat. These processes have their physical origin in the electron/phonon coupling. Numerous theoretical models have been suggested,[23] and the approximation is often made that only one vibrational (phonon) mode, the so-called accepting mode, is responsible for the quenching process.

---

(23) *Radiationless Processes, Nato Advanced Study Institutes Series B62*; edited by Di Bartolo, B., Ed.; Plenum: New York, 1979, and references therein.

This approximation has the big advantage that we can draw a configurational coordinate (CC) diagram, as shown in Figure 9, and thus visualize the situation. It allows us to correlate the nonradiative relaxation behavior with other spectroscopic properties, as we will show in the following.

For a quantitative interpretation of our lifetime data in the 200–300 K temperature range we use a model that has been successfully applied to situations that are physically similar to ours. This model is outlined in ref 24 and its application is described in ref 25 (for $Ni^{2+}$ in $LiGa_5O_8$). The nonradiative decay rate can be expressed as

$$\tau_{NR}^{-1}(T) = \tau_{NR}^{-1}(0)\exp[-S(1+2n)][(n+1)/n]^{P/2} \times \mathrm{Ip}\,[2S\sqrt{n(n+1)}] \quad (10)$$

$S$ is the Huang–Rhys factor, which is a measure of the electron–phonon coupling strength. $P$ is the number of phonons required to bridge the energy gap between the potential minima of the emitting state and the ground state. This energy gap equals the energy of the origin of the luminescence transition. It is thus observable and $P$ can be determined. Ip is a Modified Bessel function, and $n$ is the phonon population factor, which is given by

$$n = [\exp(\hbar\omega/kT) - 1]^{-1} \quad (11)$$

$n$ is also determined independently, using eq 11 and the known value of $\hbar\omega$ from Raman spectroscopy as discussed below.

Our approach in utilizing this model has thus been to reduce as far as possible the number of adjustable parameters, by calculating most of them from other experimentally available information. Before fitting the model to the nonradiative decay data, we will thus outline how the parameters were independently determined. We make extensive use of the CC diagrams for this purpose.

First we have to specify the configuration coordinate $Q$ in Figure 9, i.e., the accepting mode with frequency $\hbar\omega$ that is involved in the multiphonon relaxation. In the absence of a Jahn–Teller effect in the ground state, for which there is no clear evidence in our systems, $Q$ is the totally symmetric $TiX_6^{4-}$ breathing mode. In the pure $MgCl_2$ and $MgBr_2$ host lattices this mode has a frequency of 246[26] and 156 $cm^{-1}$,[15] respectively. The Raman spectrum of a $Ti^{2+}$-doped $MgCl_2$ crystal shows an additional peak at 260 $cm^{-1}$,[27] which we interpret as the quasi-localized $TiCl_6^{4-}$ mode of $a_{1g}$ symmetry. No Raman data are available for $Ti^{2+}$:$MgBr_2$, but we can get a good estimate by scaling down the $Ti^{2+}$:$MgCl_2$ frequency by the ratio 156/246 of the pure host lattices, giving a value $\hbar\omega_{a_{1g}} = 165$ $cm^{-1}$.

The Huang–Rhys factors are obtained from the relationship

$$S = \frac{\text{Stokes shift} - 2\hbar\omega_{av}}{2\hbar\omega_{a_{1g}}} \quad (12)$$

where the Stokes shift is the energy difference between corresponding absorption and emission maxima. Here twice the average enabling frequency ($\hbar\omega_{av}$) is first subtracted from the Stokes shift, since we are here only interested in the shift caused by gerade modes. Huang–Rhys factors $S = 3.85$ and 6.50 were thus obtained for the chloride and bromide, respectively. The shift along $Q_{a_{1g}}$ of the triplet emitting states is given by

$$\Delta Q_{a_{1g}} = (2S\hbar\omega_{a_{1g}}/k)^{1/2} \quad (13)$$

where $k$ is the force constant calculated for a harmonic oscillator. From the values of $S$ and $\hbar\omega_{a_{1g}}$ derived above we obtain $\Delta Q_{a_{1g}}$ values of 0.17 and 0.18 Å for the chloride and bromide, respectively. Taking into account the definition of $\Delta Q_{a_{1g}}$[28]

$$\Delta Q_{a_{1g}} = \sqrt{6}\Delta r \quad (14)$$

where $\Delta r$ is the change of each Ti–X distance in a $TiX_6^{4-}$ octahedron, we arrive at $\Delta r = 0.069$ and 0.073 Å values for the chloride and bromide, respectively. The positive sign of $\Delta r$ indicates that the excited state is expanded with respect to the ground state.

For the diagrams in Figure 9 we assumed harmonic potentials and the same vibrational frequencies for the ground and excited states. Both of these assumptions are usually made. For the $Ti^{2+}$:$MgCl_2$ diagram the known trigonal splitting of the $^3T_{1g}$ ground state was explicitly considered, whereas a splitting of zero was assumed for the $^3T_{2g}$ state. This assumption is based on the evidence (section IVA) that the calculated small ($\sim$100 $cm^{-1}$) splitting is further reduced by a Ham effect. We notice that the CC diagrams in Figure 9 correctly predict the luminescent state for both lattices. For $Ti^{2+}$:$MgCl_2$ we obtain an energy difference $\Delta E$ between the minima of the $^3T_{2g}$ and $^1E_g$ potentials of approximately 420 $cm^{-1}$. This compares very favorably with the value of 401 $cm^{-1}$ derived from the radiative decay studies in section IVB. The number of $a_{1g}$ phonons P required to bridge the energy gap between the $^3T_{2g}$ minimum and the ground-state minimum is 32 and 43 for the chloride and bromide, respectively.

For a quantitative fit of the experimental decay rates between 200 and 300 K the following functions were used:

$$\tau^{-1}(T) = \tau_R^{-1}(T) + \tau_{NR}^{-1}(T) \quad \text{(bromide)} \quad (15a)$$

$$\tau^{-1}(T) = \tau_R^{-1}(T) + \tau_{NR}^{-1}(T)\,P_T \quad \text{(chloride)} \quad (15b)$$

where the radiative rate $\tau_R^{-1}(T)$ is given by eq 5 for the bromide and eq 6 for the chloride with the parameters in Table II.

The nonradiative rate $\tau_{NR}^{-1}(T)$ is given by eq 10 with $\tau_{NR}^{-1}(0)$ as the only adjustable parameter. The results of these least-squares fits are shown as broken lines in Figures 7 and 8 for the chloride and bromide, respectively. The corresponding parameter values are included in Table II. An interpretation and comparison of these $\tau_{NR}^{-1}(0)$ values is very risky. In the chloride the $^3T_{2g}$ state, which provides the nonradiative pathway in the relaxation process, has no population at $T = 0$ K. This is the likely reason for the much higher value in the chloride. Much more important than these numbers, however, is the very good quality of the fit with only one adjustable parameter. It is a quantitative test for the other parameters that were determined independently. This shows that information from a variety of different measurements can be brought together to provide an overall consistent picture of the first excited states and the dominant relaxation mechanisms.

**Acknowledgment.** We thank Ch. Reber for many fruitful discussions. We are grateful to the Royal Society for a fellowship under the European Science Exchange Programme (to S.M.J.). Financial support by the Swiss National Science Foundation is gratefully acknowledged.

**Registry No.** $Ti^{2+}$, 15969-58-1; $MgCl_2$, 7786-30-3; $MgBr_2$, 7789-48-2.

---

(24) Auzel, F. In ref 23, pp 213–286.

(25) Donegan, J. F.; Bergin, F. J.; Glynn, T. J.; Imbusch, G. F.; Remeika, J. P. *J. Lumin.* **1986**, *35*, 57.

(26) Anderson, A.; Lo, Y. W.; Todoeschuck, *Spectrosc. Lett.* **1981**, *14*, 105.

(27) Jacobsen, S. M.; unpublished results.

(28) Wilson, R. B.; Solomon, E. I. *Inorg. Chem.* **1978**, *17*, 1729.